npj 2D Materials and Applications

https://doi.org/10.1038/s41699-025-00634-5

Article in Press

Enhanced polarizability and tunable diamagnetic shift from monolayer WSe_2 on relaxor ferroelectric

Received: 14 January 2025

Accepted: 7 November 2025

Cite this article as: Zhou, Q., Wang, F., Soleymani, A. *et al.* Enhanced polarizability and tunable diamagnetic shift from monolayer WSe_2 on relaxor ferroelectric. *npj 2D Mater Appl* (2025). https://doi.org/10.1038/s41699-025-00634-5

Qiaohui Zhou, Fei Wang, Ali Soleymani, Kenji Watanabe, Takashi Taniguchi, Jiang Wei & Xin Lu

Enhanced Polarizability and Tunable Diamagnetic Shift from Monolayer WSe_2 on Relaxor Ferroelectric

Qiaohui Zhou[1], *Fei Wang*[1], *Ali Soleymani*[1], *Kenji Watanabe*[2], *Takashi Taniguchi*[3], *Jiang Wei*[1], *and Xin Lu*[1*]

[1]Department of Physics and Engineering Physics,

Tulane University, New Orleans, Louisiana 70118, United States

[2]Research Center for Electronic and Optical Materials,

National Institute for Materials Science, 1-1 Namiki, Tsukuba 305-0044, Japan and

[3]Research Center for Materials Nanoarchitectonics,

National Institute for Materials Science, 1-1 Namiki, Tsukuba 305-0044, Japan.

*Xin Lu. Email: xlu5@tulane.edu.

Abstract

Strain modulation is a crucial way in engineering nanoscale materials. It is even more important for single photon emitters in layered materials, where strain can trap a delocalized exciton, leading to quantum emission. Herein, we apply strain by using the piezoelectric relaxor ferroelectric substrate. In addition to the strain-tuning of energy and polarization, we report on new observations, including the enhanced polarizability and tunable diamagnetic shift, from the charged localized excitons. As indicated from the polarization-resolved measurements, we attribute the formation of charged localized excitons to selenium vacancy defects. The shallow

defect trap, supported by the value of *g*-factor, further allows for strain-modulation of the electron-hole overlap, hence resulting in the tunable diamagnetic shift. Our results provide a new perspective in integrating layered materials with functional substrates. The contrasting features observed from the charged localized excitons also signify the prospect of charged localized emitters for quantum science and technology.

Introduction

Strain engineering provides a versatile route to modulate the properties of materials. It is particularly attractive for two-dimensional (2D) layered materials since the atomically thin thickness offers exceptional sensitivity to external perturbations. Strain tuning is even more appealing for single photon emitters (SPEs) which are formed when delocalized excitons are trapped by local defects, strain or moiré potentials in the 2D materials[1]. Strain has been demonstrated to be efficient in creating SPEs[2,3] and modulating their energies in monolayer WSe_2[4,5]. While earlier work has focused on the neutral localized excitons, less has been done for the charged localized emitters which can be controlled by chiral light due to the absence of exchange interaction and potentially work as flying qubits for the 2D spin-photon interface in quantum communication[6].

Using the inverse piezoelectric effect from a relaxor ferroelectric substrate, such as the piezoelectric $Pb(Mg_{0.33}Nb_{0.67})O_3$-($PbTiO_3$) (PMN-PT), is a well-established way for strain tuning, particularly at cryogenic temperatures. The PMN-PT substrate has been used for tuning the delocalized excitons in WSe_2, where the negatively-charged states exhibit the same tuning rate as the neutral exciton[7]. It is thus natural to expect a similar strain modulation from the charged localized excitons. Nevertheless, here we discover that the charged localized states in WSe_2 exhibit

new features on the PMN-PT substrate, in addition to showing the strain-tuning of energy and polarization. While the delocalized and neutral localized excitons exhibit negligible gate-dependent shift, the enhanced polarizability from charged localized emitters leads to a large Stark shift. We attribute the origin of charged localized excitons to selenium vacancy defects, which is corroborated by the polarization-resolved emission spectra. The magneto-optical measurement further indicates that the local potential from selenium vacancy is shallow, which enables the tunability of diamagnetic shift even under a small variation of strain (~0.05%). Our findings demonstrate the potential of coupling charged localized excitons in 2D materials with functional substrates for applications in quantum and nano optics.

Results

Independent charge and strain controls

Figure 1a depicts the schematic of a piezoelectric substrate. An external electric field parallel (anti-parallel) to the poling direction will lead to expansion (contraction) in the out-of-plane direction and compressive (tensile) strain in-plane. Compared to earlier strain-tuning studies in WSe_2[4,5,7], we added a top gate to control the doping density in WSe_2 and a front side pad (Fig. 1b). To introduce the inverse piezoelectric effect, an external voltage (*i.e.*, strain voltage) can be applied to either the back side of the PMN-PT (V_{BS}) or a front pad (V_{TS}) adjacent to the sample. Although V_{BS} is able to introduce a larger strain effect, with the presence of few-layer graphene (FLG) as the grounded contact, V_{BS} can also cause unintentional doping to the sample and may complicate the analysis, particularly when the observed features are both strain and doping dependent. We note that unintended doping is a common side effect in strain engineering[7-9], and the dual-gate geometry (with the application of top gate voltage, V_{TG}) can help to reduce such effect. A better way to dimmish the unintentional doping is to use V_{TS} which has negligible doping effect to the sample,

despite introducing a smaller strain-induced deformation (Note 1 of the Supplementary Information and Supplementary Figs. 1-4). As a result, V_{TS} is more appropriate for the study of charged excitons when carrier screening may impact the shift of energy. Before discussing the charged localized excitons, we first characterized the strain effect from our device by comparing the energy shifts of neutral excitons to previous reports[4,5]. Thanks to the rich excitonic species in WSe_2[10-12], we are able to use optical signature to identify the charge state of the sample. As shown in Fig. 1c, the presence of doublet peaks with fine structure splitting (FSS) of ~ 0.7 meV (D1 and D2 groups) - arising due to the long-range electron-hole interaction upon localization of the neutral excitons - is a signature of the neutral state. The observation of neutral localized excitons indicates that the sample is in the charge neutral regime. As V_{BS} decreased, all neutral localized excitons blue-shifted with almost the same tuning rate (Supplementary Fig. 5), which is consistent with the poling direction (Methods). Figure 1d shows that D1 shifts by ~3.2 meV for a tuning range of 400 V (8 kV/cm), which corresponds to a strain variation of ~0.05% based on an earlier experiment[13]. Although the tunability we achieved is smaller compared to the best plot in literature[4], it is comparable to the average tuning ranges shown in previous studies[4,5]. It is important to note that by improving the interfacial quality, the transferred strain from PMN-PT to WSe_2 could be enhanced[14]. As this is not the scope of our work, we will focus on the distinct features from the charged localized excitons in the following discussion.

Enhanced polarizability

Having demonstrated that our device is capable of strain-tuning at cryogenic temperature, we tuned the top gate voltage (V_{TG}) to dope the sample with electrons. Due to the Kramers' degeneracy theorem, signature of a singly charged localized exciton is the appearance of a single peak with no splitting[15]. Figure 2a, b shows the co- and cross-circularly polarized photoluminescence (PL)

spectra as V_{TG} changes from 14 V to 18 V. The presence of a single peak (labeled as S1 peak in Fig. 2a, b) with a narrow linewidth of ~300 μeV contrasts with the doublet neutral localized excitons with FSS of < 1 meV (Fig. 1c), indicating an increased carrier density in the monolayer WSe_2. We assigned the S1 peak to be a *negatively* charged localized exciton, which is supported by the V_{TG}-dependent emission intensity (stronger intensity with increasing electron density from 14 V to 17 V). A localized exciton in monolayer WSe_2 generally arises when a delocalized exciton is trapped by local strain and/or defect. Since we did not introduce local strain, e.g., via nanopillars (strain from PMN-PT is a global effect, applied to the entire WSe_2 flake), the origin of S1 peak is attributed to defect states.

To have a deeper understanding of the origin, we extracted the degree of circular polarization (DCP), defined as DCP = $(I_{co} - I_{cross})/(I_{co} + I_{cross})$, where I_{co} and I_{cross} corresponds to the co- and cross-circularly polarized emission in Fig. 2a, b. As shown in Fig. 2c, DCP is constant (0.14% ± 0.02%), independent of V_{TG}. The co-circular polarization (i.e., valley polarization) from a localized state indicates that S1 peak may originate from a selenium vacancy, because most defect states cannot preserve the threefold rotational symmetry and thus the circularly polarized emission is missing in the absence of magnetic field or magnetic proximity effect[16]. Earlier studies show that chalcogen vacancies in transition metal dichalcogenides lead to two unoccupied in-gap bands, and both consist of quasi-degenerate electronic spin-up and spin-down states[17,18]. One of the defect-induced bands from selenium vacancy is mainly localized in the K and K' valleys, the same as that for the delocalized excitons. Therefore, transition from this localized defect band to the valence band maximum is expected to exhibit circular polarization[17], which has been verified experimentally in monolayer WSe_2[18].

While selenium vacancy can explain the circular polarization, gate-dependent shift from a localized exciton is not a common feature in WSe_2[11,19,20]. As shown in Fig. 2a, b, S1 peak redshifts from ~1646 meV to ~1641 meV with V_{TG} increasing from 14 V to 18 V (see Supplementary Fig. 6 for the gate-dependent shift of S2 peak). Such large shift is unexpected due to the absence of a permanent dipole. If S1 peak originates from trapping a delocalized "bright" exciton which has an in-plane oscillating dipole, the small out-of-plane polarizability[21] is expected to suppress the quantum-confined Stark effect, as demonstrated in earlier studies[11,19,20]. On the other hand, localizing a "dark" exciton with an out-of-plane oriented dipole may lead to an observable Stark shift since the external electric field is parallel/anti-parallel to the dipole orientation[22]. Before revealing the nature of the dipole from magneto-optical spectroscopy, we first extracted the polarizability from S1 peak. To convert the change of V_{TG} ($\Delta V = 4$ V from 14 V to 18 V) to change of electric field (ΔE), we followed the work by Wang et al.[23] and connected the out-of-plane electric fields to the carrier density in WSe_2 by matching the boundary condition. The estimated ΔE scales linearly with ΔV ($\Delta E \approx 2 \times 10^6 \frac{\Delta V}{m}$) as V_{TG} increases from 14 V to 18 V when the sample is electron-doped for the entire range (Note 2 of the Supplementary Information). For the quantum dot-like localized exciton, we further applied the Lorentz local field approximation to estimate the change of local field (ΔF), $\Delta F = \Delta E(\frac{\varepsilon_w+2}{3})$[24], where $\varepsilon_w = 7.2$[25] is the dielectric constant of WSe_2. With respect to the energy at V_{TG} = 14 V, we plotted the shift of energy (ΔU) as a function of ΔF in Fig. 2d. Note that Stark shift (ΔU) is generally shown as $\Delta U = -\mu F - \frac{1}{2}\alpha F^2$, where μ is the dipole moment, α is the polarizability, and F is the electric field. As we can only estimate the relative change (ΔF), without knowing the absolute electric field (F_0) when V_{TG} = 14 V, the fitting function should be described as $\Delta U = -(\mu + \alpha F_0)\Delta F - \frac{1}{2}\alpha(\Delta F)^2$. Although we are

not able to extract the dipole moment from the linear term, the quadratic term can still reveal the out-of-plane polarizability with $\alpha = 5.7 \times 10^{-7}$ Dm/V ($1D = 3.33\times10^{-30}\, C\cdot m$) for the S1 peak. As a comparison, the out-of-plane polarizability of delocalized neutral and charged excitons in h-BN-encapsulated WSe_2 has an upper limit of ~10^{-11} Dm/V[21]. Our results indicate an enhanced polarizability from the charged localized excitons in WSe_2 on PMN-PT.

The localized excitons can be viewed as quantum-dot like structures with confinement from all three dimensions. We therefore extracted the polarizability volume of the S1 peak (α divided by $4\pi\varepsilon_0$), yielding a value of 1.7×10^4 Å^3. Note that most earlier studies do not show gate-dependent shift[11,19,20], implying an extremely small polarizability volume from the localized emitters. The only exception[26] reports that polarizability volume of localized excitons in WSe_2 typically ranges from 10 to 10^3 Å^3 (discrepancy from literature is probably due to the different dipole orientations[22]), which is at least one order smaller than our measured result. We note that the delocalized excitons and most localized neutral excitons do not exhibit gate-dependent shift, which rules out the effect from dielectric constant[27]. The enhanced polarizability volume suggests the existence of a local interaction between the PMN-PT substrate and the charged localized states in WSe_2.

As a relaxor ferroelectric, PMN-PT has domain sizes in the nanoscale (~2 to 10 nm), which is different from ferroelectric materials where domains are larger, and polarization directions are more restricted due to fewer allowed angles[28]. PMN-PT, on the contrary, contains a wide range of domain wall angles[29]. As a result, the ferroelectric polarization in PMN-PT is much weaker than that in the ferroelectrics. While the macroscopic picture excludes the ferroelectric aspect of PMN-PT, the microscopic picture, between a localized exciton in WSe_2 and a nanoscale domain in PMN-PT, could be another story. The size of a localized exciton is associated with the defect type

(generally < 10 nm)[17]. With PMN-PT being poled (Method) before sample-transfer, the domain sizes are expected to grow[30]. Despite still being small for delocalized excitons, the nanoscale ferroelectric domain may be considered as a local ferroelectric to the localized exciton, which could introduce additional tuning via ferroelectricity[31-33] and enhance the polarizability. While the localized neutral excitons are not sensitive to such tuning, our observation indicates that the local ferroelectric effect could be more influential to only certain states, such as the selenium vacancy-induced defect band which leads to the formation of S1 peak. Further magneto-optical measurements also support that the charged and neutral localized excitons from WSe_2 on PMN-PT have different origins.

Strain-dependent energy and polarization

Next, we proceeded to strain modulation by applying an electric field across the PMN-PT substrate. We used the front pad (V_{TS}) while keeping V_{TG} fixed at 17 V during the measurements. Figure 3a shows the energy of S1 peak as a function of V_{TS} in two sweeping directions (extracted from co-polarized PL spectra). The shifting direction is opposite to that in Fig. 1d (V_{BS}), since the strain voltage is applied from the front (V_{TS}). In other words, both positive V_{TS} and negative V_{BS} cause in-plane compressive (negative) strain and result in a blueshift. In Fig. 3b, we show the V_{TS}-dependent DCP, where circular polarization decreases from ~10% at -150 V to ~0% at +150 V. The same trend is reproduced from another charged localized exciton, from 25% to ~0% (see S2 peak in Supplementary Fig. 7). The polarization can be described as DCP = $\frac{G}{1+\frac{\tau_0}{\tau_s}}$, where G is the generation rate of the co-polarized excitons, and we consider $G = 1$ in our measurements. τ_0 and τ_s are the emission lifetime and spin-valley lifetime, respectively. Our observed results indicate that τ_0/τ_s increases under the compressive (negative) strain, which is opposite to the trend from delocalized excitons as shown by An et al[7]. The difference originates from the ratio of emission

lifetime and spin-valley lifetime, τ_0/τ_s. For delocalized excitons, as the radiative lifetime is short (~1 ps), the dominant depolarization path that affects DCP is the long-range exchange interaction (~ps). While the lifetimes of localized excitons are in the order of nanoseconds[34], it is crucial to consider slower processes which are insignificant for the delocalized excitons. For instance, flipping of the resident electron could occur through spin-conserving intervalley scattering or spin-flip intravalley scattering. Both would effectively reduce the spin-valley lifetime of the resident electrons, but they cannot affect DCP of the delocalized excitons (because the processes are slow, from 100 ps to tens of nanoseconds at 10 K[35]). Calculations show that compressive strain can reduce the spin nature of the lowest conduction band (where resident electrons are)[7,36], which implies that τ_s should decrease under compression. This result is consistent with our observation that τ_0/τ_s increases with negative strain.

Along with the strain-tuning effect, we also noticed that hysteresis arises in both the energy and polarization plots, which is not expected from a piezoelectric substrate. Nonetheless, hysteresis has been reported when a 2D layer is in proximity to a ferroelectric material, where PL intensities from $MoSe_2$ and WS_2 have been correlated to the adjacent ferroelectric component[32,33]. Note that the resemblance to ferroelectric tuning further supports the effect from a local ferroelectric nanodomain on the charged localized excitons.

Magnetic field-dependent energy

To better understand the nature of the localized excitons, we performed the magneto-optical measurements. Figure 4a-c demonstrates the splitting energy (ΔE) as a function of magnetic field (B) for V_{TS} = +150 V, 0 V, and -150 V. ΔE was extracted by calculating the energy difference between the split higher-energy ($P+$) and low-energy ($P-$) peaks. We fitted the data by $\Delta E = g\mu_B B$ to extract the g-factor (g), where μ_B = 58 μeV/T is the Bohr magneton. For delocalized

excitons in WSe_2, *g*-factor has distinct magnitudes for different excitonic species: it is around 4 for the bright excitons with in-plane oscillating dipoles and around 9 for the dark excitons with out-of-plane orientation[10,37,38]. However, the assignment for localized excitons is more complicated since both the in-plane and out-of-plane oscillating dipoles can display *g*-factors around 8.5[22]. We also note that it is unusual to observe $|g|$ ~4 from the localized states in WSe_2 (Supplementary Table 1).

As shown in Fig. 4a-c, the extracted *g*-factor has a magnitude around 4 for all three states, the same as that from the delocalized bright excitons, where only the orbital magnetic moments contribute to the *g*-factor ($4\mu_B$ from the valence band and that from the conduction band is zero). We can therefore exclude the contribution from the out-of-plane oriented dipole (dark exciton), as hybridization of the dark exciton should change the *g*-factor. Meanwhile, the value of *g*-factor strengthens our statement that the emission of S1 peak arises from a defect-induced band to the valence band in K/K' valley because emission involving hole in the defect level will result in a smaller $|g|$[39]. Note that stronger confinement generally leads to a larger magnitude of *g*-factor[40,41]. While $|g|$ is measured around 4, it implies that the orbital magnetic moment from the defect band is zero, and S1 peak originates from a shallow trap.

In addition to the splitting energy, we further plotted the *B*-dependent average energy of the two split peaks, which is defined as $\frac{E_{P+}+E_{P-}}{2}$. E_{P+} (E_{P-}) is the energy of the split high-energy (low-energy) peak. Both peaks are expected to shift linearly with the same magnitude but in opposite directions due to the Zeeman effect. Therefore, the average energy is expected to be constant within the range of spectral jittering. As shown in Fig. 4d, the average energy is1653.7 ± 0.1 meV from -6 T to +6 T at V_{TS} = +150 V. Nevertheless, the average energy increases by ~0.4

meV (~0.6 meV) when $|B|$ = 6 T at V_{TS} = 0 V and -150 V (Fig. 4e, f). Although diamagnetic shift can cause the average energy increases quadratically with $|B|$, a giant field is required because of the small Bohr radius of WSe_2[42]. Diamagnetic shift is defined as $\Delta E_{dia} = e^2 < r^2 > B^2/8\mu = \sigma B^2$, where $< r^2 >$ is related to the electron-hole overlap (the size of the exciton), μ is the reduced mass of the exciton (we do not expect a change of μ compared to that of the delocalized excitons because S1 peak is localized in a shallow trap), and σ is the diamagnetic shift coefficient. Theory predicts that the diamagnetic shifts are larger for charged excitons due to the increasing inter-particle distance with respect to the neutral ones. Additionally, ΔE_{dia} increases linearly with the dielectric constant of the surrounding environment[43,44]. According to the model in Ref. 43, we obtained σ = 11 μeV/T^2, resulting in $\Delta E_{dia} \sim$ 0.4 meV at $|B|$ = 6 T by taking the average dielectric constants of PMN-PT[45] and h-BN, which matches very well with the shift at V_{TS} = 0 V (Fig. 4e).

To further examine the diamagnetic shifts and strain tunability, we plotted the B-dependent E_{P+} and E_{P-} for V_{TS} = +150 V, 0 V, and -150 V in Fig. 4g-i. By including both Zeeman splitting and diamagnetic shift, the B-dependent energies of $P+$ and $P-$ are given by Equations (1) and (2), respectively.

$$\mathrm{E}(B)_{\pm} = \mathrm{E}_0 \pm \frac{|g|}{2}\mu_B B + \frac{1}{2}\sigma B^2 \quad (1)$$

$$\mathrm{E}(B)_{\pm} = \mathrm{E}_0 \mp \frac{|g|}{2}\mu_B B + \frac{1}{2}\sigma B^2 \quad (2)$$

where E_0 is the energy at B = 0 T, and $|g|$ is the magnitude of the g-factor from Fig. 4a-c. As both split peaks scale linear with B, we did not consider the contribution from diamagnetic shift for V_{TS} = +150 V (Fig. 4g). From fitting, we obtained σ = 18.8 μeV/T^2 for V_{TS} = 0 V, and σ = 37.8 μeV/T^2 for V_{TS} = -150 V (Supplementary Table 2), which indicates that the magnitude of $< r^2 >/\mu$ increases with tensile (positive) strain. Intuitively, tensile strain increases the distance between

particles and leads to a larger value of $< r^2 >$. While reduced mass is hardly affected by strain[8], the enhanced $< r^2 >$ is expected to cause a larger σ ($\sigma = e^2 < r^2 > /8\mu$). On the other hand, σ should decrease under the compressive strain, and no diamagnetic shift is expected, as shown in Fig. 4g when V_{TS} = +150 V.

We note that the strain tuning of diamagnetic shift is only present for the charged localized excitons, which could be explained by the different origins of the localized states. As shown in Supplementary Fig. 8, the extracted *g*-factor from the localized neutral exciton is ~10, which indicates that selenium vacancy defect alone could not explain the microscopic mechanism. Hybridization from the dark exciton may be required to result in this localized state. We further remark that the modulation of electron-hole overlap ($< r^2 >$), thus affecting the diamagnetic shift, benefits from the fact that our observed charged localized exciton is in a shallow trap. Charged excitons localized in a deep trap may not be able to exhibit such tunability.

Discussion

We notice that the difference between neutral and charged states is absent in earlier experimental work on quantum dots[13]. A main advantage of 2D materials is that the charged localized excitons can be in direct contact with the PMN-PT substrate, which is not possible for quantum dots. Therefore, quantum dots can only sense the global effect from strain-tuning without "seeing" the localized ferroelectric nanodomains. The importance of "direct contact" implies that one can selectively tune the electron or hole in the localized interlayer excitons by transferring a Type II heterobilayer on the piezoelectric to probe the interplay of strain and moiré potential[46]. Furthermore, we note that our applied electric field is small compared to the field required to rotate the polarization axis of the charge-neutral GaAs quantum dots[47]. Measurements with larger electric fields and magnetic fields will provide more insights into the integration of 2D layered materials

with relaxor ferroelectrics and could pave the way for potential applications in nanophotonics and quantum photonics.

Methods

Device fabrication. Electron beam lithography was used to deposit 5 nm Ti/100 nm Au metal contacts on both sides of the PMN-PT substrate. Before the sample-transfer process, the PMN-PT substrate was poled at room temperature by applying a direct current (DC) electric field to the backside. After reaching the targeted poling voltage (-300 V) in 5 minutes, we held the electric field for 30 minutes and released the field back to 0 V in 5 minutes[48]. Mechanically exfoliated WSe_2 (HQ Graphene), few-layer graphene/graphite and h-BN flakes were transferred on top of the PMN-PT substrate by a polydimethylsiloxane-based dry-transfer method[49]. The stacked device is illustrated in Fig. 1b.

Optical spectroscopy measurements. Low-temperature magneto-optical measurements were performed in a closed-cycle cryostat (AttoDry 1000, Attocube Systems) equipped with a superconducting magnet. The samples were cooled to ~3.7 K and positioned by a piezoelectric nanopositioners (Attocube Systems). Both the 633-nm and 730-nm continuous-wave excitation lasers were collimated and focused onto the sample through an objective (NA = 0.81, Attocube Systems), with a spot diameter around 1 μm. The PL emission was collected by the same objective and directed to a high-resolution spectrometer (HRS-750, Teledyne Princeton Instruments), in which it was dispersed by a 1200 g/mm grating. A charged-coupled device (PYL-400BRX, Teledyne Princeton Instruments) was used as the detector. For polarization-resolved measurements, a $\lambda/4$ waveplate was placed after the beam-splitter, and a $\lambda/2$ waveplate, followed

by a fixed-polarization analyzer, was placed before the spectrometer. Strain and top-gate voltages were applied through Keithley 6487 and Keithley 2400 source meters, respectively.

Data Availability

The data supporting the findings reported in this work are available from the corresponding author upon reasonable request.

Acknowledgement

X.L. and Q. Z. acknowledge support from Tulane University startup fund and the Louisiana Board of Regents Support Fund (BoRSF) under award # LEQSF(2022-25)-RD-A-23. K.W. and T.T. acknowledge support from the JSPS KAKENHI (Grant Numbers 21H05233 and 23H02052) and World Premier International Research Center Initiative (WPI), MEXT, Japan. J.W. and F.W. are grateful for the support from the National Science Foundation under Grant 1752997 and the Louisiana Board of Regents under Grant 082ENH-22. We also acknowledge the support from the Micro/Nano Fabrication Facility and Coordinated Instrument Facility of Tulane University.

Author Contributions

X.L. conceived the project. Q.Z. and X.L. carried out the optical spectroscopy measurements and wrote the paper, with assistance from F.W. K.W. and T.T. provided the h-BN crystals. Q.Z., F.W., and A.S. prepared the samples. X.L. and J.W. supervised the project. All authors were involved in analysis of the experimental data and contributed extensively to this work.

Competing Interests

The authors declare no competing interest.

References

1 Brotons‐Gisbert, M. & Gerardot, B. D. Quantum Photonics with 2D Semiconductors. *Photonic Quantum Technologies: Science and Applications* **2**, 563-579 (2023).

2 Branny, A., Kumar, S., Proux, R. & Gerardot, B. D. Deterministic strain-induced arrays of quantum emitters in a two-dimensional semiconductor. *Nat. Commun.* **8**, 15053 (2017).

3 Palacios-Berraquero, C. *et al.* Large-scale quantum-emitter arrays in atomically thin semiconductors. *Nat. Commun.* **8**, 15093 (2017).

4 Iff, O. *et al.* Strain-tunable single photon sources in WSe_2 monolayers. *Nano Lett.* **19**, 6931-6936 (2019).

5 Chakraborty, C. *et al.* Strain tuning of the emission axis of quantum emitters in an atomically thin semiconductor. *Optica* **7**, 580-585 (2020).

6 Atatüre, M., Englund, D., Vamivakas, N., Lee, S.-Y. & Wrachtrup, J. Material platforms for spin-based photonic quantum technologies. *Nat. Rev. Mater.* **3**, 38-51 (2018).

7 An, Z. *et al.* Strain control of exciton and trion spin-valley dynamics in monolayer transition metal dichalcogenides. *Phys. Rev. B* **108**, L041404 (2023).

8 Kumar, A. M. *et al.* Strain fingerprinting of exciton valley character in 2D semiconductors. *Nat. Commun.* **15**, 7546 (2024).

9 Hernández López, P. *et al.* Strain control of hybridization between dark and localized excitons in a 2D semiconductor. *Nat. Commun.* **13**, 7691 (2022).

10 He, M. *et al.* Valley phonons and exciton complexes in a monolayer semiconductor. *Nat. Commun.* **11**, 618 (2020).

11 Brotons-Gisbert, M. *et al.* Coulomb blockade in an atomically thin quantum dot coupled to a tunable Fermi reservoir. *Nat. Nanotechnol.* **14**, 442-446 (2019).

12 Liu, E. *et al.* Exciton-polaron Rydberg states in monolayer $MoSe_2$ and WSe_2. *Nat. Commun.* **12**, 6131 (2021).

13 Trotta, R. *et al.* Nanomembrane quantum-light-emitting diodes integrated onto piezoelectric actuators. *Adv. Mater.* **24**, 2668-2672 (2012).

14 Martín-Sánchez, J. *et al.* Strain-tuning of the optical properties of semiconductor nanomaterials by integration onto piezoelectric actuators. *Semicond. Sci. Technol.* **33**, 013001 (2018).

15 Bayer, M. *et al.* Fine structure of neutral and charged excitons in self-assembled In (Ga) As/(Al) GaAs quantum dots. *Phys. Rev. B* **65**, 195315 (2002).

16 Li, X. *et al.* Proximity-induced chiral quantum light generation in strain-engineered $WSe_2/NiPS_3$ heterostructures. *Nat. Mater.* **22**, 1311-1316 (2023).

17 Refaely-Abramson, S., Qiu, D. Y., Louie, S. G. & Neaton, J. B. Defect-induced modification of low-lying excitons and valley selectivity in monolayer transition metal dichalcogenides. *Phys. Rev. Lett.* **121**, 167402 (2018).

18 Moody, G. *et al.* Microsecond valley lifetime of defect-bound excitons in monolayer WSe_2. *Phys. Rev. Lett.* **121**, 057403 (2018).

19 Lu, X. *et al.* Optical initialization of a single spin-valley in charged WSe_2 quantum dots. *Nat. Nanotechnol.* **14**, 426-431 (2019).

20 Chakraborty, C. *et al.* 3D localized trions in monolayer WSe_2 in a charge tunable van der Waals heterostructure. *Nano Lett.* **18**, 2859-2863 (2018).

21 Verzhbitskiy, I., Vella, D., Watanabe, K., Taniguchi, T. & Eda, G. Suppressed out-of-plane polarizability of free excitons in monolayer WSe_2. *ACS Nano* **13**, 3218-3224 (2019).

22 Luo, Y., Liu, N., Kim, B., Hone, J. & Strauf, S. Exciton dipole orientation of strain-induced quantum emitters in WSe_2. *Nano Lett.* **20**, 5119-5126 (2020).

23 Wang, Z., Chiu, Y.-H., Honz, K., Mak, K. F. & Shan, J. Electrical tuning of interlayer exciton gases in WSe_2 bilayers. *Nano Lett.* **18**, 137-143 (2018).

24 Tamarat, P. *et al.* Stark shift control of single optical centers in diamond. *Phys. Rev. Lett.* **97**, 083002 (2006).

25 Kim, K. *et al.* Band alignment in WSe_2–graphene heterostructures. *ACS Nano* **9**, 4527-4532 (2015).

26 Chakraborty, C. *et al.* Quantum-confined Stark effect of individual defects in a van der Waals heterostructure. *Nano Lett.* **17**, 2253-2258 (2017).

27 Pedersen, T. G. Exciton Stark shift and electroabsorption in monolayer transition-metal dichalcogenides. *Phys. Rev. B* **94**, 125424 (2016).

28 Rojac, T. Piezoelectric response of disordered lead-based relaxor ferroelectrics. *Commun. Mater.* **4**, 12 (2023).

29 Kumar, A. *et al.* Atomic-resolution electron microscopy of nanoscale local structure in lead-based relaxor ferroelectrics. *Nat. Mater.* **20**, 62-67 (2021).

30 Qiu, C. *et al.* Transparent ferroelectric crystals with ultrahigh piezoelectricity. *Nature* **577**, 350-354 (2020).

31 Huo, D. *et al.* Tuning of the valley structures in monolayer In_2Se_3/WSe_2 heterostructures via ferroelectricity. *Nano Lett.* **22**, 7261-7267 (2022).

32 Choi, J. *et al.* Tuning exciton emission via ferroelectric polarization at a heterogeneous interface between a monolayer transition metal dichalcogenide and a perovskite oxide membrane. *Nano Lett.* **24**, 8948-8955 (2024).

33 Li, X. *et al.* Nonvolatile electrical valley manipulation in WS_2 by ferroelectric gating. *ACS Nano* **16**, 20598-20606 (2022).

34 Dass, C. K. *et al.* Ultra - Long Lifetimes of Single Quantum Emitters in Monolayer WSe_2/hBN Heterostructures. *Adv. Quantum Technol.* **2**, 1900022 (2019).

35 Ersfeld, M. *et al.* Unveiling valley lifetimes of free charge carriers in monolayer WSe_2. *Nano Lett.* **20**, 3147-3154 (2020).

36 Junior, P. E. F. *et al.* First-principles insights into the spin-valley physics of strained transition metal dichalcogenides monolayers. *New J. Phys.* **24**, 083004 (2022).

37 Liu, E. *et al.* Gate tunable dark trions in monolayer WSe_2. *Phys. Rev. Lett.* **123**, 027401 (2019).

38 Li, Z. *et al.* Direct observation of gate-tunable dark trions in monolayer WSe_2. *Nano Lett.* **19**, 6886-6893 (2019).

39 Dang, J. *et al.* Identifying defect-related quantum emitters in monolayer WSe_2. *npj 2D Mater. Appl.* **4**, 2 (2020).

40 Sheng, W. g-factor tuning in self-assembled quantum dots. *Appl. Phys. Lett.* **96**, 133102 (2010).

41 Van Bree, J., Silov, A. Y., Koenraad, P., Flatté, M. & Pryor, C. g factors and diamagnetic coefficients of electrons, holes, and excitons in InAs/InP quantum dots. *Phys. Rev. B* **85**, 165323 (2012).

42 Stier, A. V., McCreary, K. M., Jonker, B. T., Kono, J. & Crooker, S. A. Exciton diamagnetic shifts and valley Zeeman effects in monolayer WS_2 and MoS_2 to 65 Tesla. *Nat. Commun.* **7**, 10643 (2016).

43 Van der Donck, M., Zarenia, M. & Peeters, F. Excitons, trions, and biexcitons in transition-metal dichalcogenides: magnetic-field dependence. *Phys. Rev. B* **97**, 195408 (2018).

44 Stier, A. V., Wilson, N. P., Clark, G., Xu, X. & Crooker, S. A. Probing the influence of dielectric environment on excitons in monolayer WSe_2: insight from high magnetic fields. *Nano Lett.* **16**, 7054-7060 (2016).

45 Thiercelin, M., Dammak, H. & Thi, M. P. in *2010 IEEE International Symposium on the Applications of Ferroelectrics (ISAF)*, IEEE: pp 1-4 (2010).

46 Ray, A. B. *et al.* Interplay of trapped species and absence of electron capture in moiré heterobilayers. *Nano Lett.* **23**, 5989-5994 (2023).

47 Plumhof, J. D. *et al.* Strain-Induced Anticrossing of Bright Exciton Levels in Single Self-Assembled GaAs/$Al_xGa_{1-x}As$ and $In_xGa_{1-x}As$/GaAs Quantum Dots. *Phys. Rev. B* **83**, 121302(R) (2011).

48 Otoničar, M. *et al.* Effects of poling on the electrical and electromechanical response of PMN–PT relaxor ferroelectric ceramics. *Open Ceramics* 7, 100140 (2021).

49 Castellanos-Gomez, A. *et al.* Deterministic transfer of two-dimensional materials by all-dry viscoelastic stamping. *2D Mater.* **1**, 011002 (2014).

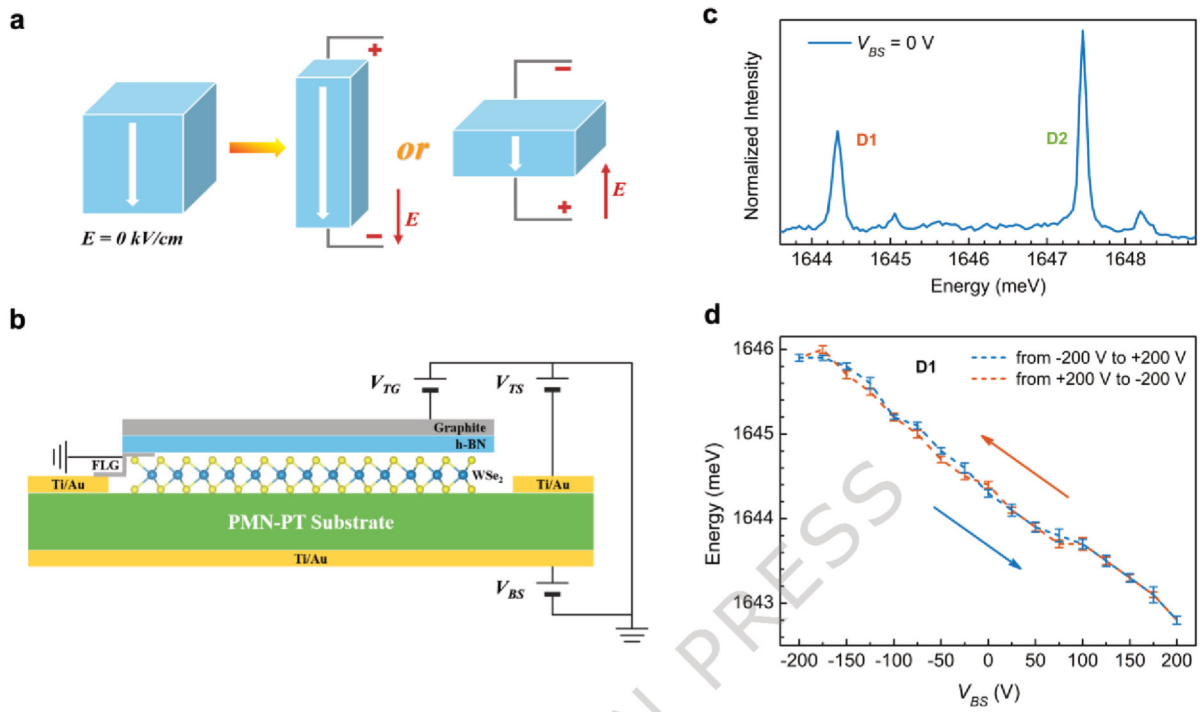

Fig. 1: **Strain-tuning of monolayer WSe_2 on a PMN-PT piezoelectric substrate. a** Sketch of a poled PMN-PT substrate with electric field applied parallel or anti-parallel to the poling direction, which produces deformations in both the out-of-plane and in-plane directions. **b** Schematic of the device consisting of graphite, hexagonal boron nitride (h-BN), monolayer WSe_2 flake, and few layer graphene (FLG) on the PMN-PT substrate. Strain voltage can be applied from the back (V_{BS}) or through an empty metal electrode on the front (V_{TS}). **c** A photoluminescence (PL) spectrum of neutral localized excitons, D1 and D2. **d** Peak energy of D1 as a function of V_{BS} from two sweeping directions. Error bars are from the mean deviation with 60 spectra taken at each V_{BS}. Excitation: 1.70 eV. Power: 150 nW.

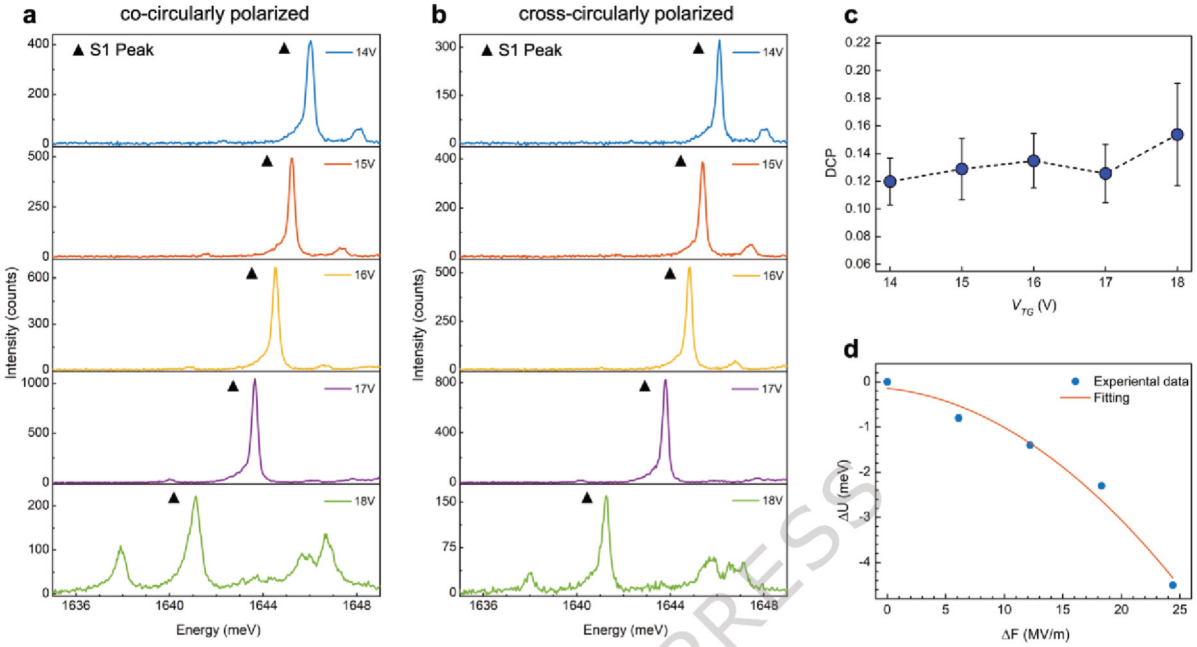

Fig. 2: **Gate-dependence of a charged localized exciton on PMN-PT. a, b** Co- and cross-circularly polarized photoluminescence (PL) spectra of a charged localized exciton, S1 peak (indicated by the triangles), as V_{TG} changes from 14 V to 18 V. Although showing up in the same measurement, other peaks in the spectra (e.g. the peak at ~1638 meV when V_{TG} = 18 V) are not peaks of interest, and we will not discuss them in the following text. **c** Degree of circular polarization (DCP) extracted from the V_{TG}-dependent PL measurements. **d** Energy shift of S1 peak (ΔU) as a function of the relative local electric field (ΔF). Fitting was done by considering the Stark effect. Error bars in **c** arise from the mean deviation of the peak intensities with more than 10 spectra taken for each voltage. Excitation for e-h: 1.96 eV. Power: 300 nW.

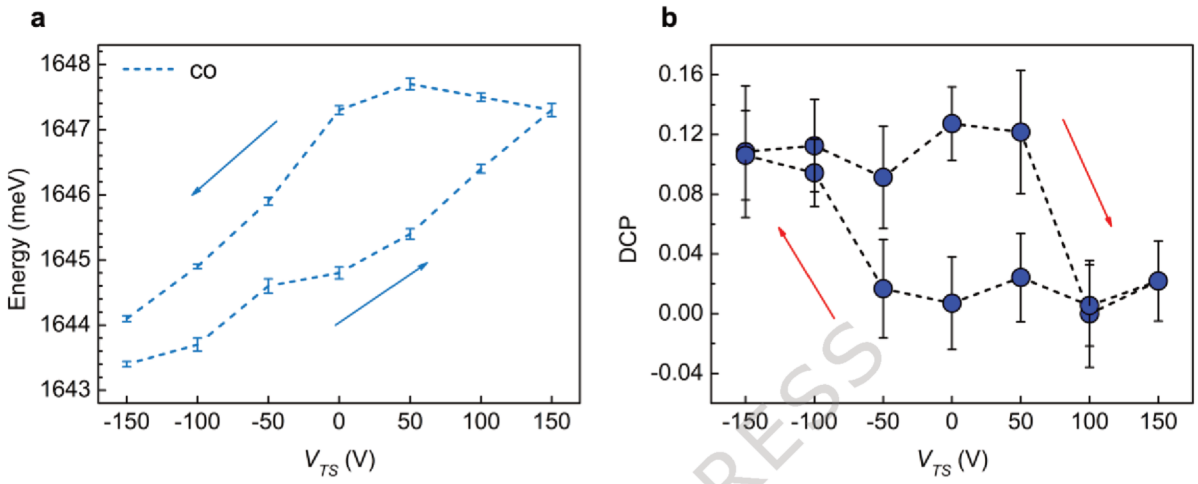

Fig. 3: Strain tuning of a charged localized exciton. a Energy shift of S1 peak as a function of V_{TS} from two sweeping directions. The peak positions were extracted from co-circularly polarized PL spectra. **b** Degree of circular polarization (DCP) from two sweeping directions. Arrows indicate the tuning directions of V_{TS}. Error bars arise from the mean deviation of the peak intensities with more than 10 spectra taken for each voltage. Excitation for e-h: 1.96 eV. Power: 300 nW.

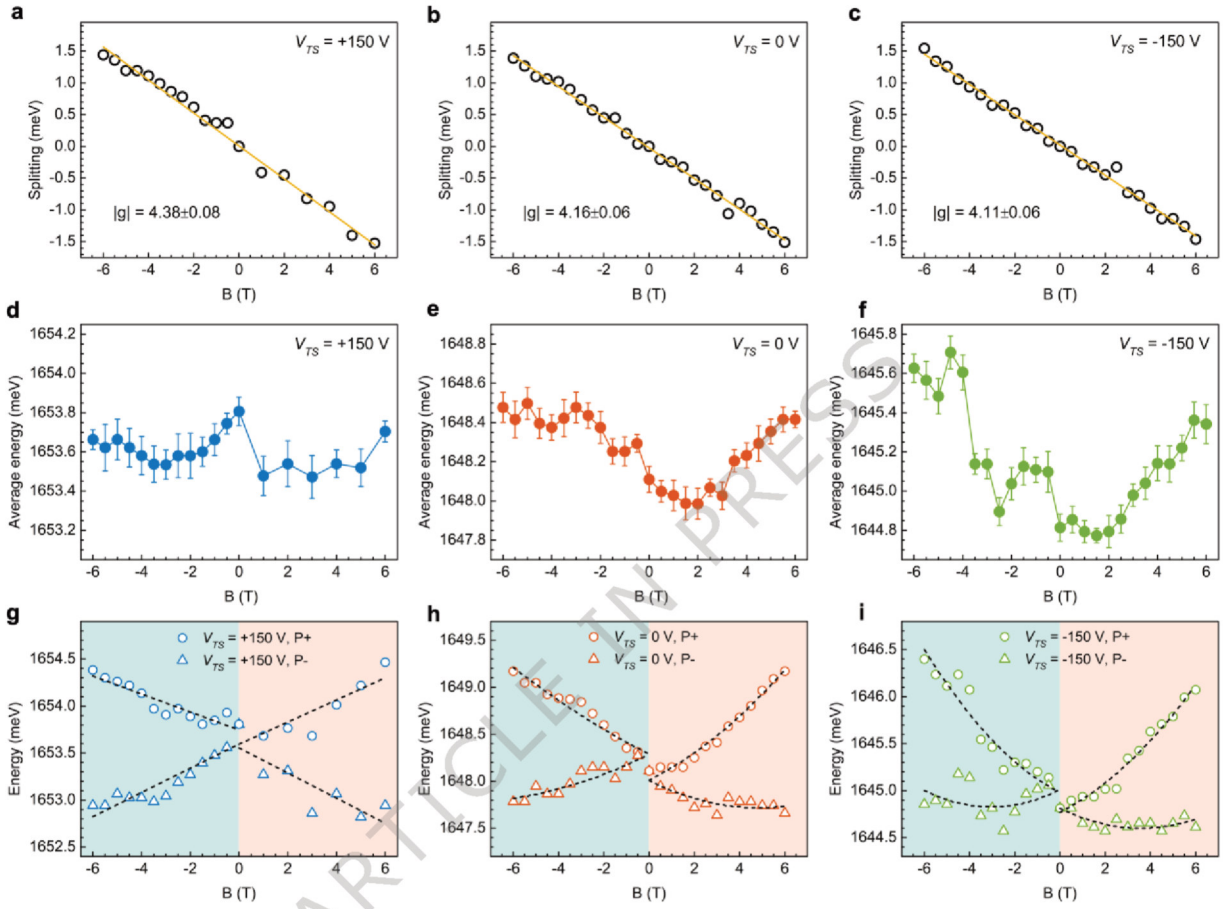

Fig. 4: **Magnetic field (*B*) dependence of S1 peak at V_{TS} = +150 V, 0 V, and -150 V. a-c** Splitting energy of S1 peak as a function of *B*. Experimental data are shown by empty dots, and fitting results are displayed by the yellow solid lines. **d-f** Average energy of S1 peak as a function of *B*. Error bars arise from spectral jittering. **g-i** *B*-dependent energy of the split high-energy (*P*+) and low-energy (*P*-) peaks. Experimental data are shown by dots/triangles, and fitting results are displayed by the black dashed lines. Excitation: 1.96 eV. Power: 300 nW.